Volcanic controls on seawater sulfate over the past 120 million years

Thomas A. Laakso[a,1], Anna Waldeck[a], Francis A. Macdonald[b], and David Johnston[a]

[a]Department of Earth and Planetary Sciences, Harvard University, Cambridge, MA 02139; and [b]Department of Earth Science, University of California, Santa Barbara, CA 93106

Edited by Thure E. Cerling, University of Utah, Salt Lake City, UT, and approved July 9, 2020 (received for review December 4, 2019)

Changes in the geological sulfur cycle are inferred from the sulfur isotopic composition of marine barite. The structure of the $^{34}S/^{32}S$ record from the Mesozoic to present, which includes ∼50- and 100-Ma stepwise increases, has been interpreted as the result of microbial isotope effects or abrupt changes to tectonics and associated pyrite burial. Untangling the physical processes that govern the marine sulfur cycle and associated isotopic change is critical to understanding how climate, atmospheric oxygenation, and marine ecology have coevolved over geologic time. Here we demonstrate that the sulfur outgassing associated with emplacement of large igneous provinces can produce the apparent stepwise jumps in the isotopic record when coupled to long-term changes in burial efficiency. The record of large igneous provinces map onto the required outgassing events in our model, with the two largest steps in the sulfur isotope record coinciding with the emplacement of large igneous provinces into volatile-rich sedimentary basins. This solution provides a quantitative picture of the last 120 My of change in the ocean's largest oxidant reservoir.

sulfur | large igneous provinces | biogeochemistry

The sulfate ion (SO_4^{2-}) is the second most abundant anion in the modern ocean. In its role as an electron acceptor and a contributor to alkalinity, it is central to the oxygen, carbon, and iron cycles on the Earth's surface. During the Cenozoic and Late Mesozoic, the marine barite ($BaSO_4$) record shows step-function–like increases in the $\delta^{34}S$ of seawater sulfate in the Eocene and Cretaceous (∼50 and 100 Ma, respectively) that seemingly violate how rapidly the sulfate reservoir should be able to change (1–5). The record also contains second-order structure that has escaped interpretation, including ∼1‰ declines in $\delta^{34}S$ before and after the Eocene and Cretaceous events. Furthermore, fluid inclusions suggest that sulfate concentrations greatly increased over this period, from a Cretaceous value of ∼2 mM to the modern value of 28 mM (6).

The major increases in the isotopic composition of seawater sulfate at ∼50 and 100 Ma have been linked to dramatic reorganizations of the carbon cycle (2, 7) or to large weathering events (3), implying significant change to the biogeochemistry of the oceans (7, 8). However, the timing and uniqueness of the proposed tectonic drivers, their elemental budget requirements, and their relationship to other features in the isotopic record remain debated. Untangling the physical processes that regulate the sulfur cycle in the ocean is critical to understanding how climate, atmospheric oxygenation, and marine ecology have coevolved over geologic time.

To address these features, we modeled the evolution of the marine sulfate concentration ($[SO_4^{2-}]$) and its isotopic composition ($\delta^{34}S$) using a forward, time-dependent model. Motivated by the combination of stepwise isotopic change and an overall increase in both sulfate concentration and $\delta^{34}S$, we drive the model with two modes of forcing: a long-term change in the background equilibrium state of seawater sulfate, and transient increases in the rate of sulfur input to the ocean. We explore the range of forcing parameters that could best explore the data, and compare the resulting optimal model to potential physical-driving mechanisms motivated by the geologic record.

Results

Our simulation of seawater $\delta^{34}S$ and $[SO_4^{2-}]$ is shown in Fig. 1, with the associated forcing shown in Fig. 2. The model is forced by a slow decrease in the efficiency with which sulfur is buried, and a parallel decrease in the isotopic composition of the outgoing sulfur (Fig. 2, *Inset*). The latter effect may represent either an increased role for isotopically depleted pyrites in total burial, or increasing fractionation during sulfate reduction. These changes lead to the slow growth in the equilibrium sulfate concentration a parallel increase in the equilibrium $\delta^{34}S$ of seawater sulfate (Fig. 1). This suite of changes may relate to any number of physical drivers. Our model represents these changes as shifts in the equilibrium sulfate concentration and $\delta^{34}S$ of seawater, and therefore does not discriminate between possible driving mechanisms. Several proposed drivers of Cenozoic geochemical cycling could lead to the required signals, as discussed below.

The remainder of the isotopic structure is generated by imposing several large pulses of sulfate into the ocean (Fig. 2). As described below, our modeled pulses have a $\delta^{34}S$ value that reflects enrichment of gas phase sulfur relative to flood basalts (1–2‰). As a result, periods forced by these input pulses are accompanied by a decrease in seawater $\delta^{34}S$, as the net S input is isotopically depleted relative to seawater. The $\delta^{34}S$ decrease is modest given the long residence time of sulfur, leading to 1–2‰ declines as seen in the barite record at ∼60 and ∼100 Ma. During this forcing, sulfate concentrations rise, causing a corresponding increase in sulfur burial rates. When the pulse ends and sulfur supply drops to its background rate, concentrations and burial

Significance

A geochemical model shows that discrete volcanic perturbations, coupled to long-term changes in sulfur biogeochemistry result in apparent stepwise changes in the isotopic composition of marine sulfur, similar to the patterns seen in the marine barite record of the Cenozoic and Late Mesozoic. The perturbations required to reproduce this isotope record in the model correlate with the timing and approximate size of large igneous provinces, particularly those intruding volatile-rich rock, suggesting that these events are responsible for much of the enigmatic structure in the sulfur isotope record of the last 120 My.

Author contributions: T.A.L., A.W., F.A.M., and D.J. designed research, performed research, analyzed data, and wrote the paper.

The authors declare no competing interest.

This article is a PNAS Direct Submission.

[1]To whom correspondence may be addressed. Email: laakso@fas.harvard.edu.

This article contains supporting information online at https://www.pnas.org/lookup/suppl/doi:10.1073/pnas.1921308117/-/DCSupplemental.

First published August 17, 2020.

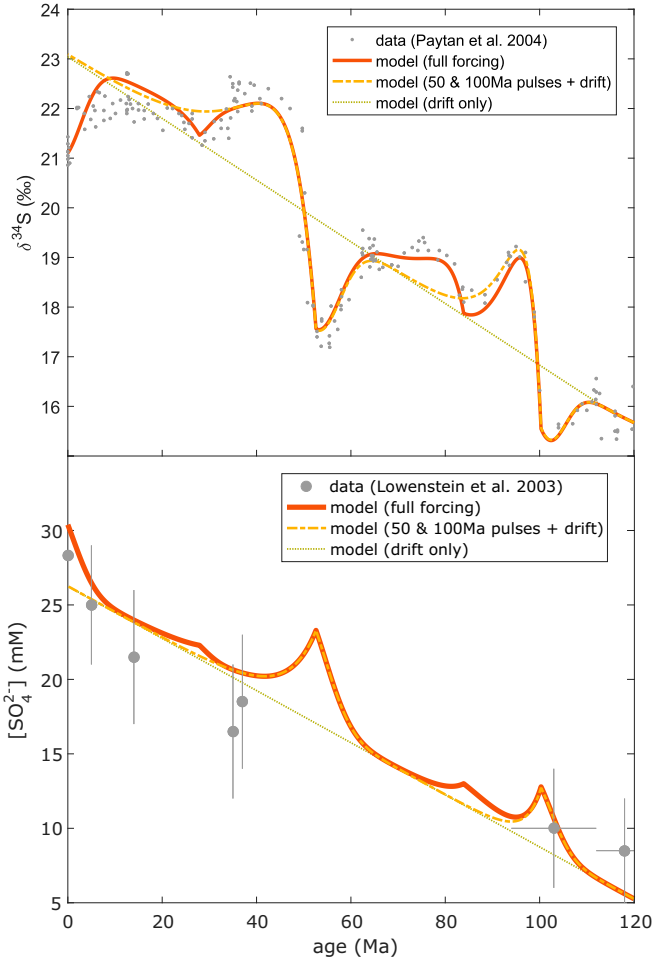

Fig. 1. The evolution of the $\delta^{34}S$ (*Top*) and concentration (*Bottom*) of marine sulfate in our model simulations of the last 120 Ma. The simulation in red includes all of the punctuated sulfur inputs shown in Fig. 2, while the simulation in yellow includes only the two events terminating at ~50 and ~100 Ma.

rates remain transiently elevated, allowing for net burial and ensuing relaxation to quasi-steady state.

Total sulfur burial is always isotopically depleted relative to seawater sulfate. Thus, net sulfur burial causes the isotopic composition of dissolved sulfate to increase during reequilibration. The "jumps" in $\delta^{34}S$ at ~50 and ~100 Ma (and potentially at ~30 and ~85 Ma) are therefore dynamic responses to reequilibration after a perturbation, rather than the direct result of a contemporaneous forcing (3, 8). This mechanism decouples the rate of change in $\delta^{34}S$ from the peak forcing, and as a result, our analysis better reproduces the maximum rate of change (e.g., at ~50 Ma) than models that drive the event with an isotopically enriched input of similar size (3). Our postperturbation relaxation is also accompanied by a characteristic isotopic "overshoot" of $\delta^{34}S$ observed in the records. And finally, as the equilibrium value of $\delta^{34}S$ has itself drifted during the perturbation, the isotopic composition of the ocean never returns to its preperturbation value. The combination of slow, secular change in the background equilibrium condition, combined with a transient forcing lasting several million years, creates the illusion of an irreversible, steplike change in sulfur cycling at ~50 and ~100 Ma.

The Role of Large Igneous Provinces. The key components of our simulation, the trend in equilibrium values and the punctuated sulfur inputs, can be linked to testable and geologically observable physical mechanisms. We first consider the hypothesized pulses of S input. We suggest these pulses represent sulfur delivered to Earth's surface by the eruption and emplacement of large igneous provinces (LIPs) into sulfur-rich sedimentary basins. Analysis of intraplate basalts suggest that ~100 Gmol of sulfur is released for every cubic kilometer of lava (9–11). Volume estimates for ancient LIPs are uncertain, with large events—including intrusives—estimated to have emplaced more than 10 million km^3 of fresh rock (*SI Appendix*). This implies total sulfur inputs on the scale of 10^{18} mol S, even before considering volatilization of sulfur adopted from intruded sedimentary rock. The timing and scale of the model pulses is simply a fit to reproduce the structure in the $\delta^{34}S$ and $[SO_4^{2-}]$ records, and thus independent of the LIP record. Without any prescribed requirement, the resulting set of modeled pulses fall within the error of fully independent geochronologic constraints on major LIPs over the past 120 Ma.

Our model of these inputs is a series of half-Gaussian pulses with average input rates between 0.2 and 0.7 Tmol S y^{-1} over characteristic timescales between 3.0–7.5 My. The slow onset and abrupt termination of our input pulses do not correspond to any particular model of LIP emplacement, although the sharply peaked behavior is consistent with geochronological data suggesting the bulk of emplacement occurs in much less than a million years (12)—notably our results are not sensitive to the exact shape of the input pulse (*SI Appendix*). Additional geochronology (e.g., ref. 13) establishing whether specific large LIPs were emplaced in less than a million years or if eruptions were spread over a longer interval may provide an important test of our model. Given the short residence time of sulfur in the atmosphere, we do not distinguish between subaerial and subaqueous eruptions, but assume that all sulfur is transferred instantly to the ocean. Total S inputs range from 0.1 to 10 Emol S, are prescribed an isotopic composition based on sulfur outgassing

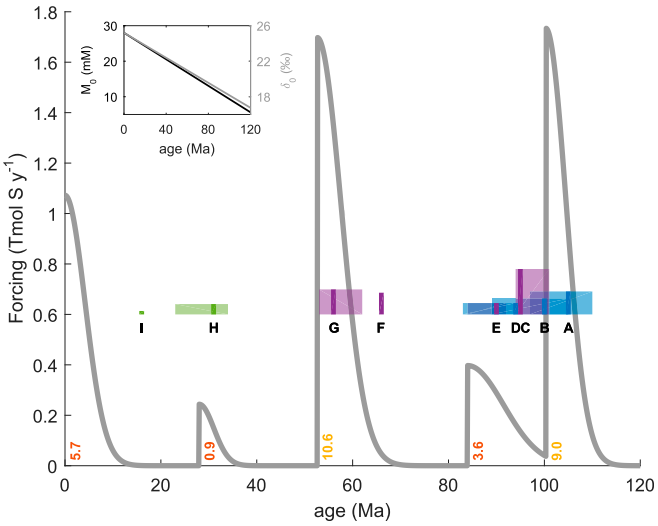

Fig. 2. The sulfur input to the ocean in excess of the background weathering rate in our simulations of the last 120 Ma. Total sulfur input over each "pulse" is given in Emol below each peak. Colored bars indicate the timing (width) and volume (height) of major large igneous provinces; the solid bar is an estimate of the peak input rate, and the transparent blocks indicate the range of ages associated with a given province. Blue indicates oceanic plateaus, green continental flood basalts, and purple volcanic margins or mixed events. *A*: Hess Rise. *B*: South Atlantic. *C*: HALIP. *D*: Caribbean-Colombian. *E*: Madagascar. *F*: Deccan. *G*: North Atlantic Igneous Province. *H*: Afro-Arabian. *I*: Columbia River. The Ontong-Java and Kerguelen plateaus have age ranges that span beyond 120 Ma and are not shown. (Inset) Evolution of the equilibrium sulfate concentration (M_0) and isotopic composition (δ_0) in the simulation.

models (1–2‰, ref. 14), and are predicted based on minimizing the model-data residual (*SI Appendix*). The resulting model of seawater $\delta^{34}S$ closely tracks the observations: the root-mean-square offset between data and model is <0.4‰, which is similar to the precision of a $\delta^{34}S$ measurement.

All of the requisite perturbations, save the Late Miocene to modern, map onto the geological distribution of LIPs (Table 1). The 53-Ma event, with total S input of 10 Emol S and an average rate of ∼0.7 Tmol S y^{-1}, broadly corresponds with the emplacement of the North Atlantic Igneous Province (63–50 Ma, peaking at ∼55 Ma with additional intrusive activity throughout the Eocene). The 100-Ma event, with total S input of 9 Emol S and an average rate of ∼0.7 Tmol S y^{-1}, broadly corresponds with the emplacement of the second pulse of the High Arctic LIP, the South Atlantic LIP, the Hess Rise, and perhaps the Kerguelen, although geochronological constraints are poor. (See Table 1 and *SI Appendix* for details on LIP ages and uncertainties). Smaller events at 84 and 28 Ma correspond to the Madagascar and Afro-Arabian LIPs. With the exception of the Deccan Traps, all of the LIPs with volumes estimated at more than 10 cubic kilometers and ages younger than 100 Ma fall within the envelope of one of the sulfur input events in our simulation (Fig. 2).

Sulfur Release during LIP Emplacement. The largest of our simulated events require more sulfur than might nominally be expected for emplacement of a given igneous province. Analysis of modern hotspots and ancient flood basalts suggests that 50–150 Gmol S are released for every cubic kilometer of lava (9–11), although the range is likely larger given uncertainty in outgassing from intrusive components and volatile release from contact metamorphism (15) as discussed below. Applying these values to total volume estimates for the North Atlantic Igneous Province (NAIP) and combined High Arctic, Hess Rise, and South Atlantic LIPs (*SI Appendix*) gives sulfur outgassing yields of 0.5–1.5 Emol S for the 50-Ma event, and 1.7–5.0 Emol for the 100-Ma event, leaving inputs too small by a factor of 2–20.

These values consider only mantle sources of sulfur, based on poorly known original volumes, and are therefore absolute minima. Volatilization of sulfur in wall rocks (14), entrainment of S in saturated magmas (16), and outgassing from silicic magmas (17) may yield as much sulfur as the basaltic magma. Importantly, the NAIP formed along an active volcanic margin and intrudes organic-rich sediments (18), and the High Arctic LIP was emplaced into oil source rocks and sulfur evaporites of the Sverdrup Basin (19). Model predictions may be satisfied if these large LIPs released abundant sulfur from shale and evaporites in wall rocks. Large LIPs that did not penetrate volatile-rich country rock, such as the Deccan Traps (20), would not have had such a large impact on the sulfur cycle. This is consistent with the stability of the isotopic record at the time of the Deccan, despite the relatively large lava volumes associated with the traps. Other large, older eruptive events that penetrate sedimentary basins, like the Permian-Triassic, record similar $\delta^{34}S$ signals as those noted here (21) and may speak to punctuated periods of massive S injections into the surface environment throughout Earth's history.

We can make a quantitative prediction for the required scale of S mobilization that our model requires by removing the potential magmatic source from the total S input needed for each event (Fig. 3). Taking the High Arctic LIP (HALIP) as an example, assuming a sulfur content of 1% and total loss of sulfur during entrainment and volatilization, our model predicts that 7.5–9.6 M km^3 of country rock would have to vent to the atmosphere. This calculated range is 150–200% the volume of the Sverdrup Basin, which the HALIP intrudes (19), but is only a quarter of the estimated volume of igneous rocks associated with the HALIP (Table 1)—that is, the HALIP intrudes a much broader region. Although total loss of sulfur during entrainment and volatilization is infeasible, intrusive rocks represent ∼80% of total LIP volume (22, 23), necessitating a substantial amount of entrainment to accommodate the intrusive rocks. In addition, metamorphic aureoles have volumes 30–250% of the intrusion itself (24), likely on the lower end for sulfur volatilization (14). Modern continental flood basalts are S saturated, and several LIPs such as the HALIP, preserve sulfide mineralization (16), suggesting the possibility of high S loss to the atmosphere and ocean. Furthermore, the Sverdrup Basin contains both oil source rocks and evaporites (19), implying that an average sulfur content of volatized wall rock higher than 1% may be appropriate. This calculation demonstrates that either a large volume or particularly S-rich sedimentary rocks are needed to drive the modeled perturbation (Fig. 3). Continued investigation of the sulfur content of intruded formations, and of the spatial scale of LIP-associated entrainment and metamorphism, will be necessary to test our proposed mechanism for sulfur release.

Furthermore, our hypothesis predicts that the average $\delta^{34}S$ of the sulfur input, including volatilized S, must be ∼0‰. The largest increases in seawater $\delta^{34}S$ in our model are transient effects produced by mass imbalance in the sulfur system. Their magnitude is therefore determined primarily by the total sulfur input, and not its isotopic composition. Given this degree of S

Table 1. Characteristics of the large igneous provinces shown in Fig. 2

LIP	Age, Ma	Setting	Target lithology	Area, Mkm^2	Volume, Mkm^3
Columbia River	16 (15.9–16.7) (12)	CFB	a	0.68 (50)	1.36 (43)
Afro-Arabia	31 (23–34) (52)	CFB	a	2.05 (42)	4.10 (–)
North Atlantic	56 (53–62) (54)	VM	b	1.07 (55)	9.90 (43)
Deccan	66 (65.5–66.5) (59)	CFB/VM	a	1.29 (42)	8.60 (43)
Madagascar	90 (84–92) (61)	CFB/OP	c	0.63 (42)	4.50 (43)
Caribbean	94 (83–94) (62)	OP	d	0.71 (42)	4.50 (43)
HALIP 2	95 (94–101) (64)	CFB/VM	b	3.60 (70)	18.00 (–)
South Atlantic	100 (89–105) (66)	OP	d	0.63 (66)	6.30 (–)
Hess Rise	105 (97–110) (67)	OP	d	0.80 (42)	9.10 (43)
Kerguelen	118 (94–120) (68)	OP/VM	d	2.30 (69)	15.10 (43)
Ontong-Java	122 (117–124) (71)	OP	d	5.20 (44)	60–90 (44)
HALIP 1	127 (120–128) (50)	CFB/VM	b	3.60 (70)	18.00 (–)

Setting abbreviations: CFB: continental flood basalt; VM: volcanic margin; OP: oceanic plateau. Lithology abbreviations: a: granite, metamorphic, and sedimentary; b: sedimentary basin; c: mixed metamorphic, basalt, and gabbro; d: basalt and gabbro. Areas are estimated original areas. When no reference is given for volume, a uniform thickness of 2 km (CFB), 5 km (VM) or 10 km (OP) was assumed. See *SI Appendix, Supplemental Text* for details and discussion of source data.

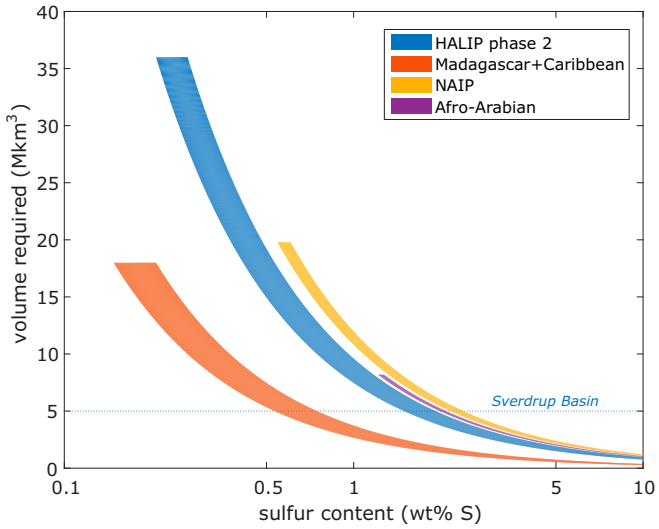

Fig. 3. The volume of country rock that must undergo entrainment or S volatilization in order to produce the sulfur inputs required for each of the events in our model (Table 2), assuming 100% loss of sulfur to the atmosphere. The width of each curve results from uncertainty in the magmatic S released during LIP formation (see main text). Solutions requiring volumes larger than twice the volume of the LIP (Table 1) are not shown. The approximate volume of the Sverdrup Basin (ref. 19), intruded by the HALIP, is shown for reference.

input, its composition must be ~0‰ in order to produce the observed "dips" in seawater $\delta^{34}S$ before the "spikes" (see *SI Appendix*, Fig. S8). This holds for both the major events in our model. These calculations suggest that, if volatilized sedimentary sulfur is an important component of S input, it must be composed of either relatively enriched sulfide phases (e.g., ref. 8), or a combination of depleted sulfides and enriched sulfate minerals. While the largest events in our model, the NAIP and HALIP, intrude both organic rich and evaporite deposits (18, 19), a detailed sulfur isotopic examination of the intruded rock awaits future work.

Additional constraints on the outgassing and volatilization rates might be derived from contemporaneous changes in the carbon cycle (*SI Appendix*, Fig. S1); however, the weak carbon isotope response from mantle-derived CO_2 (25), coupled to the variability in C and S release from magmas and volatilized wall rocks, makes a quantitative prediction challenging. Similarly, a coupling between seawater Sr and S is complicated by continental input of Sr. An increased flux of volcanic S should be coupled with the input of nonradiogenic Sr to the surface, depressing seawater Sr isotope values. However, the release of CO_2 associated with LIPs causes a transient increase in silicate weathering, leading to more radiogenic Sr isotope values on <1-My timescales, as seen across the P-T boundary (26), until a return to steady-state CO_2 associated with the silicate weathering feedback. On the 10^7-year timescale of LIP removal (27), weathering of ^{87}Sr-poor LIP extrusive lavas will depress strontium isotope ratios in seawater (28). Superimposed on the broad rise in Sr isotope values associated with exhumation of radiogenic crust during the breakup of Pangea (e.g., ref. 28) and the Himalayan orogeny, there are deflections in the rise at ~105, 90, 65, and 15 Ma that could conceivably be associated with LIPs. Thus, the duration change in Sr weathering input is likely to be long and variable compared to the dynamic response of the S isotope system to the termination of volcanism, resulting in the observed weak coupling of $^{87}Sr/^{86}S$ to $\delta^{34}S$ (*SI Appendix*, Fig. S1).

The proposed LIP mechanism does not explain the $\delta^{34}S$ trend from Miocene to present. The Columbia River Flood Basalt is the most recent LIP, but it is too small to account for the required sulfur inputs (~7 Emol S), unless intrusions into Cenozoic basins are larger than currently estimated (12). This suggests that other aspects of the sulfur system are also important in determining the isotopic composition of the ocean, such as changes in the provenance of weathered sulfur or redox-mediated changes in sulfide burial rates. More broadly, the smaller events in our simulation (28 and 84 Ma) may not be the only plausible explanations for the finer structure observed in the data around these ages. However, the large events at ~50 and ~100 are consistent with the timing of the NAIP and HALIP, explain much of the variance in the data including some aspects of the secondary structure, and do so without relying on a large number of fitting parameters.

A test of this model comes with new data through the millions of years preceding the current study interval. The first pulse of the HALIP at ~127 Ma was followed by peak Ontong Java plateau emplacement at ~122 Ma (29) and by the Kerguelen LIP at ~118 Ma. Combined, these are an order of magnitude larger than younger LIPs, and both the HALIPs and Kerguelen LIPs invaded potentially volatile-rich basins. These events should drive a transient drop in seawater $\delta^{34}S$ (30), and our hypothesis posits a subsequent overshoot and recovery (Fig. 4), with the latter potentially delayed until ~100 Ma by emplacement of the Hess Rise, Southeast Atlantic, and second pulse of the HALIP. There is a significant data gap during this period (31), but seawater $\delta^{34}S$ declines rapidly at the start of the record, suggesting either recovery from the ~135-Ma Parana LIP, or a fundamentally different steady state compared to the last 120 Ma. Indeed, our proposed drift in the equilibrium value of $[SO_4^{2-}]$ over time cannot be extrapolated backward indefinitely without reaching zero sulfate concentrations, suggesting that, while our model accurately reproduces the last 120 Ma of data, additional controls are at play earlier in Earth history. Nevertheless, as this data gap is filled the modeled response to emplacement of these volcanic provinces (Fig. 4) will provide an important test of the link between LIPs and seawater sulfur isotopes.

Longer-Term Change in the S Cycle. The second component of our model is the coupled long-term drift in $\delta^{34}S$ and $[SO_4^{2-}]$. We propose these trends are the result of a decrease in the efficiency of sulfur burial at an average rate of ~1% per million years. This could be the result of both pyrite and sulfate burial becoming less efficient, with a 15% increase in the pyrite:sulfate burial ratio leading to the observed increase in $\delta^{34}S$ (25). Alternatively, the increase in $[SO_4^{2-}]$ may have been due to declining efficiency of pyrite burial alone. In this case, the average fractionation between pyrite and sulfate must have increased by ~10‰ to explain the observed increase in $\delta^{34}S$ (*Materials and Methods*). Such an increase is observed in the geological record (32), but is not supported by microbial mechanisms alone (33). Rather, this signal may relate to contraction of shallow-water environments like epicontinental seas (8), which are likely characterized by rapid pyrite burial and smaller pyrite fractionations (8). pH-mediated changes in precipitation kinetics (34) associated with changes in seawater chemistry (35) could also play a role in altering pyrite formation rates. An overall decrease in precipitation rates may have encouraged sulfide migration and reoxidation, particularly in regions with large sulfide gradients, leading to both lower rates of pyrite burial and a redistribution toward sites with lower reduction rates and larger ^{34}S fractionation. This remains an important area for future study.

Conclusions

Our results suggest that volcanic forcing associated with LIPs can explain much of the structure in the $\delta^{34}S$ record of seawater sulfate when coupled to slow changes in the equilibrium values of $[SO_4^{2-}]$ and $\delta^{34}S$. Other tectonic drivers for S isotope change

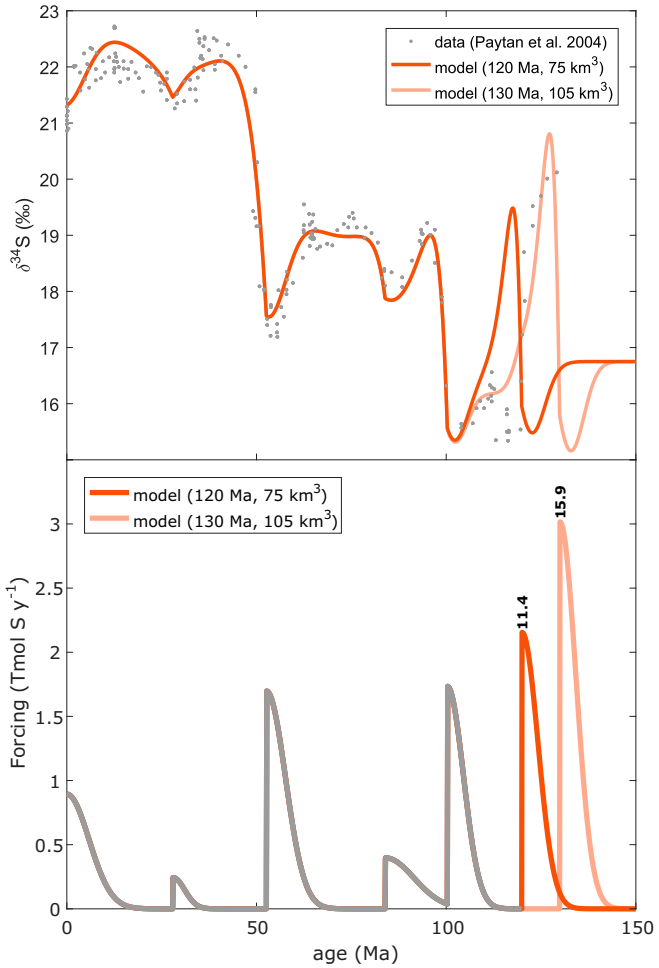

Fig. 4. The evolution of the $\delta^{34}S$ of marine sulfate in model simulations of the last 150 Ma (*Top*). The simulations include the LIP forcings shown in Fig. 2, and forcing from an additional LIP event representing the combined Ontong-Java and Kerguelen Plateaus (*Bottom*). Two pulses, each representing a different model of the combined Ontong-Java and Kerguelen Plateaus, are shown in red, with the forcing from Fig. 2 shown in gray. Total sulfur input over each pulse is given in Emol (10^{18} moles) above each peak. The pulse peaking at 120 Ma uses the lower-bound volumes given in Table 1; the pulse peaking at 130 Ma uses the upper-bound volumes. Note that a peak at 130 Ma is earlier than is suggested by the record (Table 1), and is instead chosen to approximately fit the barite record before 120 Ma. Prior to 120 Ma, the equilibrium parameters δ_0 and M_0 are held at their 120-Ma values (*Materials and Methods*).

(arc–continent collision, ridge subduction, basin formation/destruction) occur commonly and on ∼10-My timescales (36); satisfying the marine sulfate record requires more punctuated, unique, ∼1-My sulfur inputs (1–3, 7, 8). Overall, our hypothesis is consistent with geologic observations of large volcanic events intruding into volatile-rich basins, and is in contrast to the permanent, steplike changes in sulfur cycling previously proposed (1, 7, 8). Thus, despite its central role in biogeochemical cycles, seawater sulfate may serve at the whim of the solid Earth.

Materials and Methods

Consider a one-box ocean with a dissolved sulfate reservoir of M moles and isotopic composition $\delta^{34}S \equiv \delta$. The sulfur fluxes out of the ocean are assumed to be first-order processes with rate constants k_i, and the sulfur input is divided between a constant "background" weathering flux of F_W, and any time-dependent variations around that rate, F':

$$\frac{d}{dt}M = F_W + F' - \sum_i k_i M \quad [1]$$

$$\frac{d}{dt}(\delta M) \approx \delta_W F_W + \delta' F' - \sum_i \delta_i k_i M \quad [2]$$

$$\Rightarrow \frac{d}{dt}\delta \approx (\delta_W - \delta)\frac{F_W}{M} + (\delta' - \delta)\frac{F'}{M} - \sum_i \varepsilon_i k_i, \quad [3]$$

where δ_W and δ' are the isotopic compositions of the sulfur fluxes F_W and F', respectively, and ε_i is the average isotopic offset of a given sulfur precipitate relative to seawater. Solving for steady state while setting the variable input F' to zero defines the equilibrium reservoir size and isotopic composition:

$$M_0 \equiv \frac{F_W}{\sum_i k_i}, \quad [4]$$

$$\delta_0 \equiv \delta_W - \frac{\sum_i \varepsilon_i k_i}{\sum_i k_i}. \quad [5]$$

These terms represent an equilibrium state toward which the ocean will relax in the absence of forcing (F'), and if ε_i and k_i remain constant. The latter condition does not need to be true, and thus the values of δ_0 and M_0 can vary over time. Such behavior would cause M and δ to evolve in time even in the absence of any input forcing, F'. M_0 and δ_0 do in fact vary over time in our simulations, following linear trends described in *SI Appendix*. Note that while this parameterization does require choices for the values of M_0 and δ_0 over time, it is agnostic as to the physical parameters that give rise to those values via Eqs. **4** and **5**. In other words, it is not necessary to specify any of the global rate constants or average fractionation terms.

The original time-sensitive equations can be expressed in terms of the equilibrium parameters, eliminating any explicit dependence on the rate constants and fractionations.

$$\frac{d}{dt}M = \left(1 - \frac{M(t)}{M_0}\right)F_W + F', \quad [6]$$

$$\frac{d}{dt}\delta = (\delta_W - \delta)\frac{F_W}{M(t)} - (\delta_W - \delta_0)\frac{F_W}{M_0} + (\delta' - \delta)\frac{F'}{M(t)}. \quad [7]$$

In the absence of forcing F', the reservoir size M evolves as a simple first-order relaxation toward its equilibrium value, M_0. The evolution of δ is more complex, even without the forcing terms, due to interactions with a potentially changing reservoir size. For example, if sulfate levels are transiently elevated ($M >> M_0$), the rate of change in δ approaches a constant value of $\Sigma_i(\varepsilon_i k_i)$, representing the dominant effect of reservoir size-dependent (and thus transiently large) burial fluxes over the fixed weathering input.

The equations are solved by Eulerian integration with a time step of 10^5 years following a 10-My spin-up with the equilibrium constants M_0 and δ_0 extended backward in time from their 120-Ma values using the trends shown in Table 2. Note that, because the ocean is evolving toward an equilibrium condition that is itself drifting over time, neither δ nor M are exactly equal to δ_0 or M_0 at 120 Ma. Following this spin-up, these equilibrium

Table 2. Parameters for the pulses of sulfur input used in the simulation described in the main text and shown in Fig. 2

Parameter	Description	Units	#1	#2	#3	#4	#5
τ_i	Age of peak input	Ma	0.0	28.0	52.6	84.0	100.4
σ_i	Pulse width	My	5.8	3.1	5.0	7.5	4.2
A_i	Total input	Emol S	6.6	0.9	10.6	3.6	9.0
δ'_i	$\delta^{34}S$ of input	‰	1.0	1.0	2.0	1.0	2.0
b_δ	δ_0 at 120 Ma	‰			16.75		
b_M	M_0 at 120 Ma	mM			5.6		
m_δ	Rate of change δ_0	‰/120 Ma			8.45		
m_M	Rate of change M_0	mM/120 Ma			22.4		

"constants" are allowed to vary linearly in time, representing possible changes in the globally averaged values of the burial rate constants or fractionation factors.

The time-varying forcing flux, F', consists of a series of pulses with the S input rate Gaussian-distributed in time, but truncated to zero input at any time more recent than the age of peak input, and less recent than three standard distributions from that age:

$$F'_j = \begin{cases} 0 & \text{if } t \le \tau_j - 3\sigma_j \\ \frac{A_j}{\sqrt{2\pi\sigma_j}} e^{-\frac{(t-\tau_j)^2}{2\sigma_j^2}} & \text{if } \tau_j - 3\sigma_j < t \le \tau_j \\ 0 & \text{if } t > \tau_j \end{cases} \quad [8]$$

where j denotes a particular forcing "event," of which there may be more than in a given simulation. The isotopic composition of this input is fixed at a constant value.

We initially sought a simulation that could fit the data using only linear variations in the equilibrium parameters (M_0, δ_0) and a pair of forcing events F' with peaks at $\tau = 50$ and 100 Ma This requires a choice of the background weathering rate and isotopic composition, and a slope (m) and 120-Ma value (b) for both equilibrium parameters and a set of amplitudes (A), timescales (σ), and isotopic compositions (δ') for each of the events, given in Table 2. Following this initial manual tuning, we ran a brute-force search over values of the forcing parameters (τ, A, σ, δ') centered on the initial values. For each parameter combination, we integrated the mass and isotope equations from 120 Ma to present, evaluating the quality of the simulation by taking the root mean square of the deviations between the fit and each point in the barite data set from Paytan et al. (1). The solution with the smallest value of this metric is shown in Figs. 1 and 2. Following this exercise, we repeated this process using the "optimized" fit as a baseline and cumulatively added forcings initially centered at 0, 30, and 87 Ma in order to produce the five-pulse simulation shown in Fig. 1. The resulting pulse parameters are given in Table 2. We explored use of alternative age models for the barite data (30) and found that the optimized forcings had magnitudes that differed by less than 10%, and peak ages that differed by less than a few million years when compared to our baseline model shown in Figs. 1 and 2.

The observed long-term trends in sulfate concentration and isotopic composition can be fit to linear variations in the equilibrium terms M_0 and δ_0 as described above. In physical terms, this must represent changes in at least two of the quantities that define these equilibrium values (Eqs. **6** and **7**): the sulfur weathering rate, F_W, the first-order rate constants for sulfur burial k, and the isotopic fractionations associated with sulfur burial ε. It is possible to solve for the required rates of changes by choosing values for the rate of change in M_0 and δ_0 based on the barite and fluid inclusion data, and then taking the derivative of Eqs. **6** and **7** with respect to time and assuming any two of the terms are time-varying. For example, explaining the trend with covariations in $k_{sulfate}$ and k_{pyrite} leads to a drop in sulfate burial from 2.1 to 1.7 Tmol y^{-1} over the simulation, with pyrite burial rising from 0.7 to 1.1 Tmol y^{-1} (*SI Appendix*, Fig. S2). Alternatively, a decline in pyrite burial can be coupled to a decline in e_{pyr} from 55‰ to about 40‰ (*SI Appendix*, Fig. S3).

The optimization procedure described above does not allow for variation in the trends in these equilibrium terms. The result of lifting this restriction is explored in *SI Appendix*, Fig. S4. Alternative choices in the initial value and trend in δ_0 can improve the fit to the barite data over portions of the record, but results in notably poor fits over other portions. Ultimately a linear trend is an artificial choice unlikely to reflect reality, but this simple choice allows the model to capture and explore the physical mechanisms suggested here—slow drift in either k or ε—with the fewest possible degrees of freedom.

The barite record of δ extends back to 129 Ma, close to the emplacement of the largest known LIP, the Ontong-Java (OTJ) Plateau, whose date of emplacement also overlaps with the large Kerguelen Plateau (Table 1). Extrapolation of the linear drift terms back to these dates results in near-zero sulfate concentrations (or infinite burial rate constants), suggesting that the processes driving this drift no longer apply in the Middle Cretaceous. To explore this time period, we fix the δ_0 and M_0 at their 120-Ma values, run the model to equilibrium, and then apply a single sulfur input pulse based on estimates of the age and combined rock volume for the OTJ and Kerguelen (Table 1), using the upper-bound sulfur content discussed in the main text. We then allow the age of the plateau to vary within a few million years in order to find a superior fit. We also consider a manual adjustment of the age of the combined event by several million years.

Data Availability. The model code used in this study is available in GitHub at https://github.com/tomlaakso/s120Ma. No new data was produced as part of this study.

ACKNOWLEDGMENTS. Support was provided by Harvard University (A.W., D.J., and T.A.L.), NSF Marine Geology and Geophysics OCE-1821958 (D.J. and A.W.), NSF Frontiers in Earth Science Grant 1926001 (F.A.M.), and NASA Exobiology NNX15AP58G (D.J.).

1. A. Paytan, M. Kastner, D. Campbell, M. H. Thiemens, Seawater sulfur isotope fluctuations in the Cretaceous. *Science* **304**, 1663–1665 (2004).
2. A. C. Kurtz, L. R. Kump, M. A. Arthur, J. C. Zachos, A. Paytan, Early Cenozoic decoupling of the global carbon and sulfur cycles. *Paleoceanography* **18**, 1090 (2003).
3. U. G. Wortmann, A. Paytan, Rapid variability of seawater chemistry over the past 130 million years. *Science* **337**, 334–336 (2012).
4. A. L. Masterson, B. A. Wing, A. Paytan, J. Farquhar, D. T. Johnston, The minor sulfur isotope composition of Cretaceous and Cenozoic seawater sulfate. *Paleoceanography* **31**, 779–788 (2014).
5. T. J. Algeo, G. M. Luo, H. Y. Song, T. W. Lyons, D. E. Canfield, Reconstruction of secular variation in seawater sulfate concentrations. *Biogeosciences* **12**, 2131–2151 (2015).
6. T. K. Lowenstein, L. A. Hardie, M. N. Timofeeff, R. V. Demicco, Secular variation in seawater chemistry and the origin of calcium chloride basinal brines. *Geology* **31**, 857–860 (2003).
7. A. V. Turchyn, D. P. Schrag, Oxygen isotope constraints on the sulfur cycle over the past 10 million years. *Science* **303**, 2004–2007 (2004).
8. V. C. F. Rennie *et al*., Cenozoic record of $\delta^{34}S$ in foraminiferal calcite implies an early Eocene shift to deep-ocean sulfide burial. *Nat. Geosci.* **11**, 761–765 (2018).
9. Th. Thordarson, S. Self, Sulfur, chlorine, and fluorine degassing and atmospheric loading by the Roza eruption, Columbia River Basalt Group, Washington, USA. *J. Volcanol. Geotherm. Res.* **74**, 49–73 (1996).
10. Th. Thordarson, S. Self, N. Óskarsson, T. Hulsebosch, Sulfur, chlorine, and fluorine degassing and atmospheric loading by the 1783-1784 AD Laki (Skaftár Fires) eruption in Iceland. *Bull. Volcanol.* **58**, 205–225 (1996).
11. B. A. Black, L. T. Elkins-Tanton, M. C. Rowe, I. U. Peate, Magnitude and consequences of volatile release from the Siberian Traps. *Earth Planet. Sci. Lett.* **317-318**, 363–373 (2012).
12. J. Kasbohm, B. Schoene, Rapid eruption of the Columbia River flood basalt and correlation with the mid-Miocene climate optimum. *Science Adv.* **4**, eaat8223 (2018).
13. C. G. Kingsbury, S. L. Kamo, R. E. Ernst, U. Söderlund, B. L. Cousens, U-Pb geochronology of the plumbing system associated with the Late Cretaceous Strand Fiord Formation, Axel Heiberg Island, Canada: Part of the 130-90 Ma High Arctic large igneous province. *J. Geodyn.* **118**, 106–117 (2018).
14. C. Yallup, M. Edmonds, A. V. Turchyn, Sulfur degassing due to contact metamorphism during flood basalt eruption. *Geochim. Cosmochim. Acta* **120**, 263–279 (2013).
15. A. Parmigiani, W. Degruyter, S. Leclaire, C. Huyber, O. Bachmann, The mechanics of shallow magma reservoir outgassing. *Geochem. Geophys. Geosyst.* **18**, 2887–2905 (2017).
16. D. H. C. Wilton, B. M. Saumur, A. Gordon, M. C. Williamson, Enigmatic massive sulphide mineralization in the high Arctic large Igneous Province, Nunavut, Canada. *Can. J. Earth Sci.* **56**, 790–801 (2019).
17. B. Scaillet, R. Macdonald, Experimental and thermodynamic constraints on the sulphur yield of peralkaline and metaluminous silicic flood eruptions. *J. Petrol.* **47**, 1413–1437 (2006).
18. H. Svensen *et al*., Release of methane from a volcanic basin as a mechanism for initial Eocene global warming. *Nature* **429**, 542–545 (2004).
19. A. Embry, B. Beauchamp, "Sverdrup basin" in *The Sedimentary Basins of the United States and Canada*, A. Miall, Ed. (Elsevier, 2019), pp. 559–592.
20. L. M. E. Percival *et al*., Does large igneous province volcanism always perturb the mercury cycle? Comparing the records of Oceanic Anoxic Event 2 and the end-Cretaceous to other Mesozoic events. *Am. J. Sci.* **318**, 799–860 (2018).
21. S. M. Bernasconi *et al*., An evaporite-based high-resolution sulfur isotope record of Late Permian and Triassic seawater sulfate. *Geochim. Cosmochim. Acta* **204**, 331–349 (2017).
22. B. M. Saumur, K. Dewing, M. C. Williamson, Architecture of the Canadian portion of the High Arctic Large Igneous Province and implications for magmatic Ni-Cu potential. *Can. J. Earth Sci.* **53**, 528–542 (2016).
23. S. M. White, J. A. Crisp, F. J. Spera, Long-term volumetric eruption rates and magma budgets. *Geochem. Geophys. Geosys.* **7**, Q03010 (2006).
24. I. Aarnes, H. Svensen, J. A. D. Connolly, Y. Y. Podladchikov, How contact metamorphism can trigger global climate changes: Modeling gas generation around igneous sills in sedimentary basins. *Geochim. Cosmochim. Acta* **74**, 7179–7195 (2010).
25. B. Hannisdal, S. E. Peters, Phanerozoic Earth system evolution and marine biodiversity. *Science* **334**, 1121–1124 (2011).
26. C. Korte, H. W. Kozur, P. Bruckschen, J. Veizer, Strontium isotope evolution of late Permian and triassic seawater. *Geochim. Cosmochim. Acta* **67**, 47–62 (2003).

27. Y. Park, N. Swanson-Hysell, L. Lisiecki, F. A. Macdonald, "Evaluating the relationship between the area and latitude of large igneous provinces and Earth's long-term climate state" in *Environmental Change and Large Igneous Provinces: The Deadly Kiss of LIPs*, R. E. Ernst, Ed. (American Geophysical Union, 2020) In press.
28. Y. Goddéris *et al*., Paleogeographic forcing of the strontium isotopic cycle in the Neoproterozoic. *Gondwana Res.* **42**, 151–162 (2017).
29. B. Taylor, The single largest oceanic plateau: Ontong Java-Minihiki-Hikurangi. *Earth Planet. Sci. Lett.* **241**, 372–380 (2006).
30. J. V. Mills *et al*., Massive volcanism, evaporite deposition, and the chemical evolution of the Early Cretaceous ocean. *Geology* **45**, 475–478 (2017).
31. B. Kristall, A. D. Jacobson, B. B. Sageman, M. T. Hurtgen, Coupled strontium-sulfur cycle modeling and the Early Cretaceous sulfur isotope record. *Palaeogeogr. Palaeoclimatol. Palaeoecol.* **496**, 305–322 (2018).
32. W. D. Leavitt, I. Halevy, A. S. Bradley, D. T. Johnston, Influence of sulfate reduction rates on the Phanerozoic sulfur isotope record. *Proc. Natl. Acad. Sci. U.S.A.* **110**, 11244–11249 (2013).
33. A. Masterson, M. J. Alperin, W. M. Berelson, D. T. Johnston, Interpreting multiple sulfur isotope signals in modern anoxic sediments using a full diagenetic model (California-Mexico margin: Alfonso Basin). *Am. J. Sci.* **318**, 459–490 (2018).
34. D. Rickard, G. W. Luther 3rd, Chemistry of iron sulfides. *Chem. Rev.* **107**, 514–562 (2007).
35. A. G. Dunlea, R. W. Murray, D. P. Santiago Ramos, J. A. Higgins, Cenozoic global cooling and increased seawater Mg/Ca via reduced reverse weathering. *Nat. Commun.* **8**, 844 (2017).
36. F. A. Macdonald, N. L. Swanson-Hysell, Y. Park, L. Lisiecki, O. Jagoutz, Arc-continent collisions in the tropics set Earth's climate state. *Science* **364**, 181–184 (2019).